RESEARCH

Open Access

Effective path-loss compensation model based on multipath exploitation for through-the-wall radar imaging

Florian Mkemwa[1], Abdi T. Abdalla[1], Baraka Maiseli[1*], Idrissa Amour[2] and Ali Muqaibel[3]

*Correspondence:
barakaezra@udsm.ac.tz

[1] Department of Electronics and Telecommunications Engineering, College of Information and Communication Technologies, University of Dar es Salaam, 14113 Dar es Salaam, Tanzania
[2] Department of Mathematics, College of Natural and Applied Sciences, University of Dar es Salaam, 16103 Dar es Salaam, Tanzania
[3] Electrical Engineering Department, and Center of Communication Systems and Sensing, King Fahd University of Petroleum and Minerals, 31261 Dhahran, Saudi Arabia

Abstract

Through-the-wall radar imaging (TWRI) has attracted a great deal of attention in several sensitive applications, including rescue missions and military operations. Notwithstanding its broad range of applications, TWRI suffers from path-loss because distant targets experience more attenuation of signal power than those closer to the transceiver. This challenge may lead to missed targets with important information necessary for analysis and informed decision making. Responding to the challenge, we have developed a signal model with an effective path-loss compensator incorporating a free space exponent. Furthermore, multipath exploitation and compressive sensing techniques were employed to develop an effective algorithm for isolating residual clutter that may corrupt real targets. The proposed signal model integrates contributions from the front wall, multipath returns, and path-loss. Compared with the state-of-the-art model under the same experimental conditions, simulation results show that the proposed model achieves improved signal-to-clutter ratio, relative clutter peak, and probability of detection by 13.1%, 17.4% and 33.6%, respectively, suggesting that our model can represent the scene more accurately.

Keywords: Compressive sensing, Multipath exploitation, Path-loss compensator, Through-the-wall radar imaging

1 Introduction

Through-the-wall radar imaging (TWRI) is used to detect obstructed targets behind the walls. TWRI involves imaging the interior parts of a building to detect, identify, classify and track the whereabouts of humans and other desired targets. This technology may be useful in rescue missions (e.g., recovering people from fire and earthquake tragedies) and military operations [1–4]. Recently, there has been notable achievements in TWRI with authors establishing robust methods and techniques to advance the field [5–16].

TWRI suffers from multipath reflections and path-loss that cause poor accuracy in target detection [17–21]. The former factor originates from surrounding walls and near targets that tend to produce ghosts (replicas of the genuine targets) during image reconstruction. Multipath ghosts cause scene cluttering that reduces the probability for accurate target detection, classification, and localization [1, 22]. Path-loss describes

the reduction in power density of the electromagnetic wave as it propagates from the transceiver to the desired target. This process occurs during imaging of the behind-the-wall scene. Since free space path-loss varies with frequency and distance travelled by the electromagnetic wave, distant targets undergo more path-loss than near targets. If not effectively mitigated, path-loss may have substantial impact on target detection, especially on distant targets with weaker reflectivities. Consequently, the scene may not be accurately represented [17, 18].

Reverberation from the front wall may be another serious challenge that negatively impacts reconstruction of scenes in TWRI. Consequently, ghosts become equally spaced along the downrange because of multiple reflections from outer and inner surfaces of the wall. Moreover, strong reflections within the wall cause near targets to be masked out [18, 22]. Many TWRI applications require highly resolved radar images, which can only be achieved with large apertures and wide bandwidths. These requirements present yet another challenge of bigger sensing measurements that pose computational complexities and increased processing time [23, 24].

Researchers have devised multiple methods to address the challenges in TWRI. To alleviate the effects of multipath reflections, scholars have developed techniques that broadly fall into two categories: aspect-dependent based and multipath-exploitation based. The former technique is based on the finding that, when a scene is interrogated from different radar locations, the corresponding ghosts' locations change while the true targets remain at the same pixels [1, 25]. The later technique exploits additional energy from multipath reflections by focusing the energy to the real targets. This technique requires complete knowledge of the reflective geometry of the scene, and can be used with compressed sensing (CS) [22] or without CS [26]. When used with CS, multipath exploitation suppresses the ghosts thoroughly by inverting the multipath model [22]. The front wall effects are counteracted using relevant mitigation methods, such as spatial filtering [27] and singular value decomposition [28]. To address the big data challenge, CS is usually employed to reconstruct a sparse signal using only a small fraction of linear projections of the original signal without compromising the image quality [24, 29–31]. Despite these noteworthy efforts, path-loss effects have not been adequately mitigated in TWRI.

Most works in TWRI assume that path-loss is absorbed into the complex reflectivity of the target. This assumption is unrealistic because path-loss stems from the physical effects of electromagnetic wave propagation. Alahmed et al. [17] considered path-loss and proposed a path-loss compensator that recouped the effect of free space path-loss to two targets in the presence of the front wall. However, multipath returns were not considered in their model. Kokumo et al. [18] extended the work of Alahmed et al. [17] by incorporating multipath returns in the design of the path-loss compensator. However, the model by Kokumo et al. resulted in highly cluttered images. Notwithstanding the limitation, and considering a category of methods pursued along the current research trajectory, this model remains the most recent one with promising performance. Therefore, we have used the Kokumo et al.'s model for benchmarking and comparison.

In this paper, we apply the multipath exploitation under the CS framework to develop a compensation model that recoups path-loss more efficiently. The proposed model effectively applies a free space path-loss as the fundamental component for the

Mkemwa *et al. EURASIP Journal on Advances in Signal Processing*   (2023) 2023:42

Page 3 of 18

compensator. We factor in multipath returns and introduce a clutter isolation algorithm. These modifications and improvements ensure that all behind-the-wall targets are accurately detected. Our novelty seats on the proposed clutter isolation algorithm that considers the established compensation model to generate high quality images with little clutter. This algorithm opens promising research avenues to implement superior TWRI approaches into practical systems, an achievement that may save lives of people trapped in hazardous natural disasters. We should note that TWRI is still an evolving field with several prospects for real-world realization.

The remainder of this paper is organized as follows. In Sect. 2, the TWRI signal model is presented. Section 3 describes the proposed path-loss compensation model and Sect. 4presents the path-loss compensated received signal model. In Sect. 5, the simulation setup and results are presented. Section 6concludes the study.

2 TWRI signal model

TWRI scene interrogation requires a stepped-frequency radar to maintain high energy of the transmitted ultra-wideband signal. This strategy improves the down-range resolution [1, 26, 32]. Furthermore, crossrange resolution increases with aperture length, and this improvement in resolution gives a reason why recent TWRI systems employ Synthetic Aperture Radar [27, 32]. Consider a stepped frequency signal, realized by N radar locations and a series of M monochromatic waves with uniform frequency spacing, used to image a scene in which front wall reflections, internal wall multipath, and interaction multipath exist [22]. Figure 1 illustrates a scene model showing first-order multipath returns while imaging a typical TWRI scene. Suppose that the scene is subdivided into $N_x \times N_y$ pixels along crossrange and downrange, respectively. The received signal corresponding to the mth frequency ($m = 0, 1, \ldots, M - 1$) and n^{th} transceiver location ($n = 0, 1, \ldots, N - 1$) is obtained by combining the front wall returns, $y_w[m, n]$, target returns, $y_t[m, n]$, target interactions, $y_i[m, n]$, and ambient noise sample, $\upsilon[m, n]$, and can be expressed as [18]

$$y[m, n] = y_w[m, n] + y_t[m, n] + y_i[m, n] + \upsilon[m, n]. \tag{2.1}$$

If specular reflection is assumed, and if the reflectivity of a target at the pth pixel is σ_p, where $p = 0, 1, 2, 3, \ldots, N_x N_y - 1$, the received signal is given as [4]
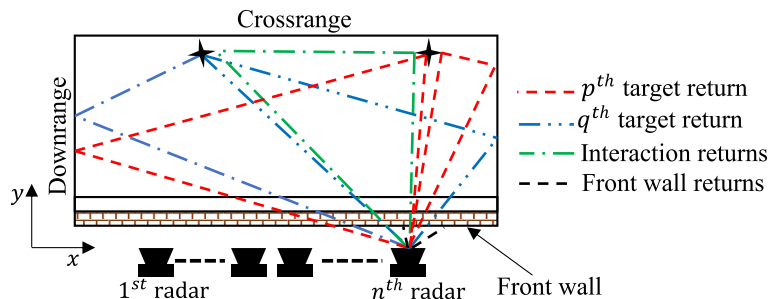

Fig. 1 Signal model for through-the-wall radar imaging

$$
\begin{aligned}
y[m,n] = & \sum_{r_w=0}^{R_w-1} \sigma_w^{(r_w)} \exp(-j2\pi f_m t_w^{(r_w)}) \\
& + \sum_{r=0}^{R-1} \sum_{p=0}^{N_x N_y-1} \sigma_p^{(r)} \exp(-j2\pi f_m t_{pn}^{(r)}) \\
& + \sum_{p,q=0,p\neq q}^{N_x N_y-1} \sigma_{pq} \exp(-j2\pi f_m t_{pqn}) + \upsilon(m,n),
\end{aligned}
\tag{2.2}
$$

where R represents the number of target returns, σ_w and σ_p are wall and target reflectivities in relation to r_w^{th} and r^{th} returns, respectively. Also, t_{pn} is the round-trip delay between p^{th} target and n^{th} receiver due to the rth return. Similarly, t_{pqn} denotes the round-trip delay between the targets, p and q, with respect to the nth receiver for the rth return, while $t_w^{(r_w)}$ signifies delay from the front wall.

3 Proposed path-loss compensation model

This work proposes a path-loss compensation model that can more effectively recoup the path-loss effects. Contrary to the conventional two-step approach (Fig. 2a), the proposed model compensates path-loss attenuation in three steps (Fig. 2b): firstly, the uncompensated (intermediate) image is formed, followed by estimation of the possible locations of targets; secondly, using the estimated target location vector, the selective pixel-wise path-loss compensation is performed; lastly, the final image is reconstructed from the compensated measurements. For the second step, our work presents a clutter isolation algorithm that facilitates the estimation of target locations and the construction of a selective compensation matrix.

One of the shortcomings of the existing models is that path-loss is compensated for every pixel, even for the pixels unoccupied by targets. This shortcoming suggests that contributions from clutter will also be amplified and, consequently, the final image will have low signal-to-clutter ratio (SCR) and low relative clutter peak (RCP). In the current work, we propose a clutter isolation algorithm that addresses this shortcoming by ensuring that only a few selected pixels with presumed targets are compensated. Since the locations of targets are unknown, the intermediate image is used to estimate such locations.

The idea of estimating the locations originates from the premise of TWRI: returns from pixels occupied by targets are stronger because targets have higher reflectivities. During image formation, the intensity of each pixel is normalized to the maximum
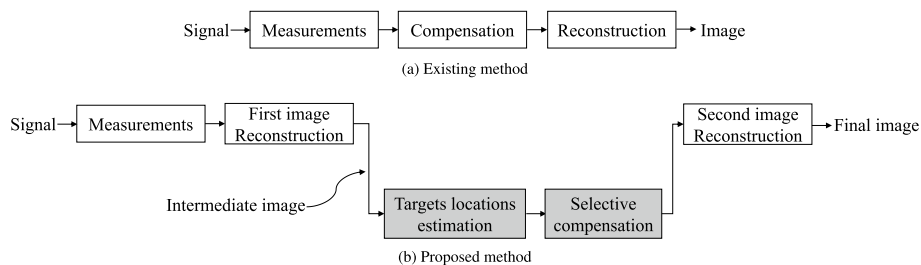

Fig. 2 Path-loss compensation method

intensity. Therefore, targets are reasonably assumed to reside in pixels of highest values of normalized intensity.

Prior information on the number of targets behind the wall may be known or unknown [1, 33]. When the number of targets, k, is known, the algorithm sorts the elements of the image vector in a descending order. This process retrieves k largest values of normalized intensity and their corresponding indices in the original image vector. The indices represent k pixels (locations) occupied by k targets. Let k and $\hat{s}_i$ be the number of targets and the intermediate image vector, respectively. Then, the resulting target vector, h, can be expressed as $h = [h_1, h_2, h_3, \ldots, h_k]^T$ where $h_1, h_2, h_3, \ldots, h_k$ are the k largest elements of $\hat{s}_i$ with $h_k = |\hat{s}_{ik}|$. The target location vector that contains the assumed target locations corresponding to h is given by $l = [l_1, l_2, l_3, \ldots, l_k]^T$, where $l_1, l_2, l_3, \ldots, l_k \in [1, 2, 3, \ldots, N_x N_y]$ and l_k is the index of h_k in $\hat{s}_i$.

For the unknown number of targets, estimation can be done from the available parameters of the imaging system. Scholars have established that, assuming scene sparsity, the number of targets in high resolution images is small compared with the number of pixels [23]. Therefore, for a given pixel grid of size $N_x N_y$, if a small constant, γ, representing the fraction of pixels occupied by targets is selected such that $k << N_x N_y$, the maximum number of targets, k, becomes

$$k = \gamma N_x N_y. \tag{3.1}$$

Once k is obtained, the location of the assumed targets is calculated the same way as for the known number of targets. Next, the compensation matrix is constructed for strategic pre-processing of the measurements. Specifically, the matrix compensates path-loss to simultaneously achieve higher values of SCR and RCP in the final reconstructed image.

The free space path-loss is quantified as

$$L = \frac{(4\pi d f)^2}{G_t G_r c^2}, \tag{3.2}$$

where G_t and G_r denote transmit and receive antenna gains, respectively, f represents the signal frequency, and d is the distance between the transmitter and the receiver. The equation

$$L(m, n, p) = (t_{pn} f_m)^2 \tag{3.3}$$

derived from (3.2) is used to compute entries of the compensation matrix. $L(m, n, p)$ represents path-loss experienced by the radar return for the mth frequency at the nth location by the pth pixel. The derivation of (3.3) is shown in the Appendix. The algorithm to isolate clutter from compensation is summarized in Algorithm 1.

Algorithm 1: Clutter isolation algorithm

Input : Intermediate image vector, $\hat{s}_i$, number of targets, k
Output: Selective compensation matrix, G

1 Check whether the number of targets is known
2 If the number of targets, k, is known, sort elements of $\hat{s}_i$ in a descending order to obtain k
  largest elements of $\hat{s}_i$, $h_1, h_2, h_3, \ldots, h_k$, with $h_k = |\hat{s}_i|$
3 If the number of targets, k, is unknown, estimate the maximum number of targets in a given
  pixel-grid while leveraging sparsity of the scene; $k = \gamma \times N_x N_y$. Sort elements of $\hat{s}_i$ in a
  descending order to obtain k largest elements of $\hat{s}_i$, $h_1, h_2, h_3, \ldots, h_k$, with $h_k = |\hat{s}_i|$
4 Find pixels corresponding to $h_1, h_2, h_3, \ldots, h_k$ elements of $\hat{s}_i$. This step gives the location of
  targets represented by $l_1, l_2, l_3, \ldots, l_k \in [1, 2, 3, \ldots, N_x N_y]$, where l_k is the index of h_k in $\hat{s}_i$
5 Build the compensation matrix, G, which compensates only the pixels in Step 4, in which
  targets are presumed to be residing

---

4 Path-loss compensated received signal model

Since our focus is to compensate path-loss for target returns, we assume that front wall contributions in (2.1) have already been suppressed using the techniques by Lagunas et al. [27] and Tivive et al. [28]. To compensate for path-loss, $y[m, n]$ is multiplied by a compensator, $g(m, n, p)$, for the mth frequency, n^{th} radar location, and p^{th} pixel to yield a path-loss compensated return

$$
\hat{y}[m, n] = \sum_{p=0}^{N_x N_y - 1} g(m, n, p) y_t[m, n, p]
$$

$$
+ \sum_{p=0}^{N_x N_y - 1} g(m, n, p) y_i[m, n, p] + \hat{v}[m, n]. \tag{4.1}
$$

With R multipath returns from interior walls, (4.1) becomes

$$
y[m, n] = \sum_{r=0}^{R-1} \sum_{p=0}^{N_x N_y - 1} \sigma_p^{(r)} \exp(-j2\pi f_m t_{pn}^{(r)}) g^{(r)}(m, n, p)
$$

$$
+ \sum_{p,q=0, p \neq q}^{N_x N_y - 1} \sigma_{pq} \exp(-j2\pi f_m t_{pqn}) g(m, n, p) + \hat{v}(m, n). \tag{4.2}
$$

For notational simplicity, we can reasonably vectorize (4.2) such that the *MN* measurements in $y[m, n]$ are stacked to form a tall vector [22]

$$
\hat{y} = [\hat{y}[0, 0], \ldots, \hat{y}[M - 1, 0], \ldots, \hat{y}[M - 1, N - 1]]^T. \tag{4.3}
$$

Similarly, the reflectivities are expressed in vector form as

$$
\boldsymbol{s}^{(r)} = \left[\boldsymbol{\sigma}_0^{(r)}, \boldsymbol{\sigma}_1^{(r)}, \ldots, \boldsymbol{\sigma}_{N_x N_y - 1}^{(r)} \right]. \tag{4.4}
$$

The phase terms for target and interaction returns are represented by dictionary matrices $\boldsymbol{\Phi}$ and $\boldsymbol{\psi}$, respectively, defined by

$$\left[\boldsymbol{\Phi}^{(r)}\right]_{zp} = \exp(-j2\pi f_m t_{pn}^{(r)}) \tag{4.5}$$

and

$$\left[\boldsymbol{\psi}^{(r)}\right]_{zp} = \exp(-j2\pi f_m t_{pqn}), \tag{4.6}$$

where $z = 0, 1, \ldots, MN - 1$, $m = i \mod M$ and $n = \lfloor i/M \rfloor$. After obtaining the target location vector, $\boldsymbol{l}$, selective compensation is achieved by the matrix equation

$$\left[\boldsymbol{G}^{(r)}\right]_{zp} = \begin{cases} \left(t_{pn}^{(r)} f_m\right)^2, p \in \boldsymbol{l} \\ 1, p \notin \boldsymbol{l} \end{cases} \tag{4.7}$$

As indicated in (4.7), the matrix compensates path-loss only if the pixel contains a target, otherwise, the corresponding return is not compensated. Consequently, clutter caused by all-pixel compensation is suppressed.

Applying CS to the received compensated signal yields [23]

$$\bar{\boldsymbol{y}} = \boldsymbol{D}\tilde{\boldsymbol{y}} = \boldsymbol{C}^{(0)}\boldsymbol{s}^{(0)} + \boldsymbol{C}^{(1)}\boldsymbol{s}^{(1)} + \ldots + \boldsymbol{C}^{(R-1)}\boldsymbol{s}^{(R-1)} + \boldsymbol{C}_i\boldsymbol{s}_i + \boldsymbol{v}, \tag{4.8}$$

where $\boldsymbol{C}^{(r)} = \boldsymbol{D}(\boldsymbol{G}^{(r)} \circ \boldsymbol{\Phi}^{(r)})$, $\boldsymbol{C}_i = \boldsymbol{D}(\boldsymbol{G}^{(0)} \circ \boldsymbol{\psi}^{(r)})$, $\boldsymbol{D} \in \{0, 1\}^{J \times MN}$, and $r = 0, 1, \ldots R - 1$. Considering the first target in target interactions to be the perfect reflector [34], (4.8) can be re-written as

$$\bar{\boldsymbol{y}} = \boldsymbol{C}\hat{\boldsymbol{s}} + \boldsymbol{v} \tag{4.9}$$

with $\boldsymbol{C} = \boldsymbol{C}^{(0)} + \boldsymbol{C}^{(1)} + \ldots + \boldsymbol{C}^{(R-1)} + \boldsymbol{C}_i$. Equation (4.9) is a basis pursuit denoising problem, which is solved using YALL1 [35] by mixed ℓ_1/ℓ_2-norm regularization, to recover the unknown image vector $\hat{\boldsymbol{s}}$.

5 Results and discussions

For fair comparison, we maintained the room layout, simulation setup, and radar imaging parameters used in the recently proposed model [18]. The origin of the coordinate system is selected to be at the center of the array. The front wall is located parallel to the array at 0.5 m, and had a thickness of 20 cm and a relative permittivity, ϵ, of 7.6632. The first sidewall (sidewall 1) is positioned at -1.83 m and the second sidewall (sidewall 2) is positioned at 4 m, while the backwall stands at 6.37 m. Three point targets were randomly placed at $(0.31, 3.60)$ m, $(-0.62, 5.20)$ m, and $(0.71, 1.00)$ m (Fig. 3).

The imaging parameters were set as follows: stepped frequency signal, $f = 1$ GHz to 3 GHz; $M = 101$ frequency bins; $N = 45$ transceiver locations with equal-weighted multipath; $R = 4$. The scene is discretized into 45×45 pixels. Additive White Gaussian Noise of SNR 0 dB was added to the measurements and the simulation results were obtained using MATLAB R2018a.

For proper benchmarking, the simulation was carried out using the Delay-and-Sum Beamforming (DSBF) technique that utilizes all measurements [36]. Then, CS was used and only half of the frequency bins and half of the transceiver locations were randomly selected. CS sparse image reconstruction was done using YALL1 algorithm as recommended by AlBeladi and Muqaibel [37]. The simulation was performed with two and
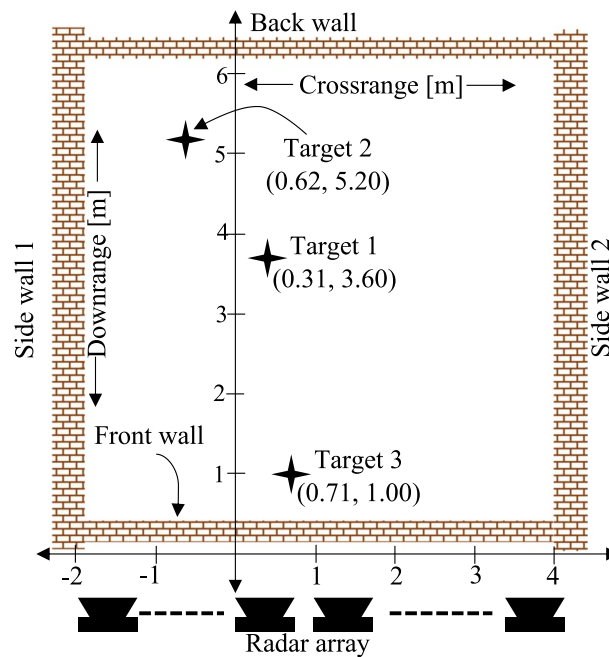
Mkemwa *et al. EURASIP Journal on Advances in Signal Processing*   (2023) 2023:42

Page 8 of 18

Fig. 3 Room layout for measurements

three targets to further validate the performance of our model. Moreover, simulation was done by considering scenarios with known and unknown number of targets.

The metrics that were used to quantify performance of the proposed model were probability of detection, PD (which is similar to recall rate [37] and matching rate [19]), SCR and RCP. In addition, the images obtained from simulating the models were evaluated through qualitative analysis.

5.1 Two targets scenario

Figures 4b through d show images formed using DSBF with full measurement scene data. The path-loss effect manifests itself in Fig. 4b where the far target appears with diminished intensity compared with the original scene depicted in Fig. 4a. The resulting images from the existing and the proposed models are shown in Figs. 4c and d, respectively. Evidently, the proposed model recouped path-loss effects more effectively. To quantify the improvement, PD, SCR and RCP were computed. PD refers to the ratio of the number of detected targets to the total number of targets. The PD against normalized intensity threshold is shown in Fig. 5. The intensity of one signifies that the target was perfectly reconstructed. Ideally, the PD should be 100% (all targets detected) across the entire intensity threshold range, (0-1). The line graph in Fig. 5 shows that, for the uncompensated case, the PD fell to 50% (one target detected) beyond 0.5 intensity threshold. The Figure further shows that, in the existing model, the PD dropped to 50% for values of intensity above 0.7, and that the proposed model yielded a PD of 100% till the 0.9 intensity, where it fell to 50%.

SCR values obtained were 27.92 dB, 28.09 dB, and 28.22 dB for uncompensated case, existing model, and proposed model, respectively. RCP values were 2.86 dB, 2.31 dB, and 0.67 dB for the uncompensated, existing, and proposed (compensated) cases,
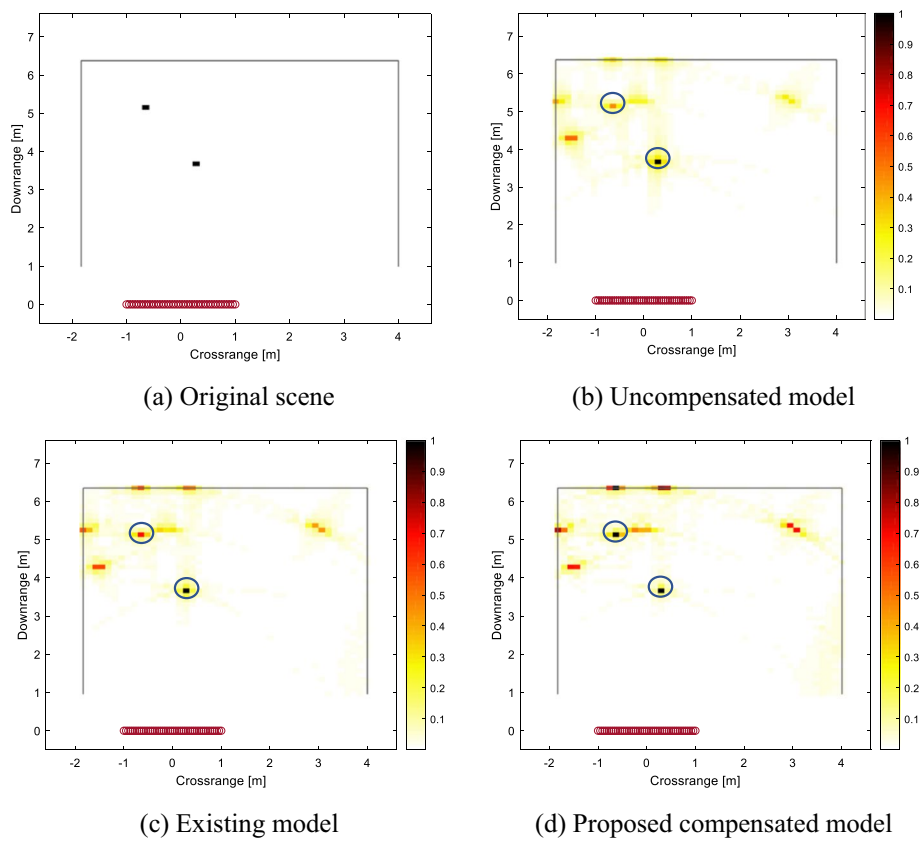
(a) Original scene   (b) Uncompensated model

(c) Existing model   (d) Proposed compensated model

Fig. 4 Images from Delay-and-Sum Beamforming in two targets scenario
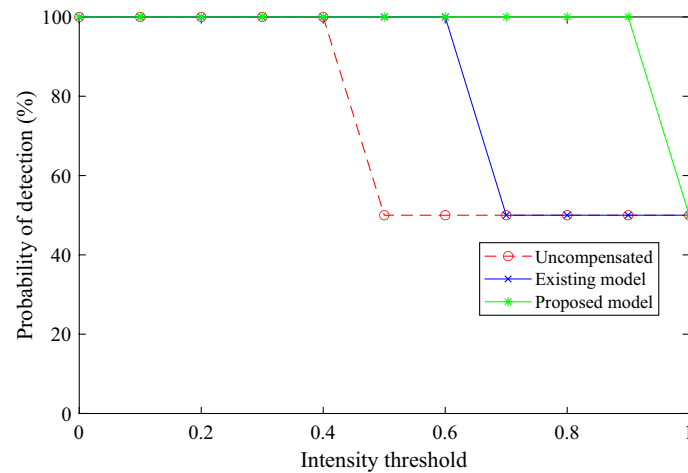

Fig. 5 Probability of detection vs intensity threshold with DSBF

respectively. In DSBF, ghosts are not suppressed, thus degrading SCR and RCP of the image.

Simulations using CS with only 25% of the original data volume were performed in two scenarios, known and unknown number of targets. Figure 6a shows the image obtained when path-loss was not compensated. In this case, the second target was not detected

(a) Uncompensated model

(b) Existing model

(c) Proposed (compensated) model

(d) Probability of detection
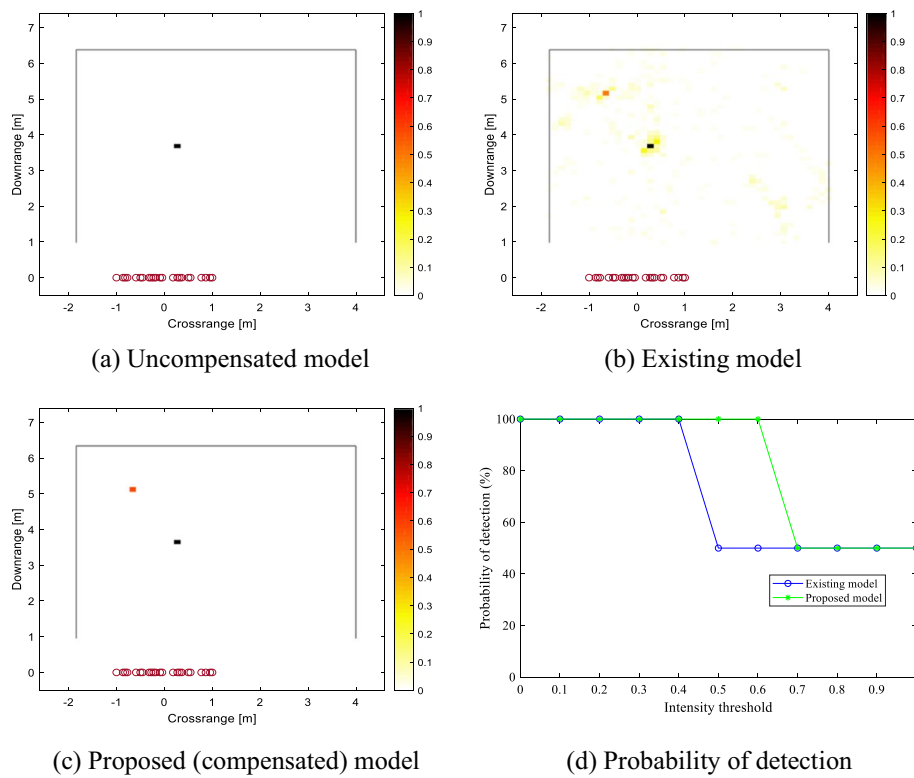
Fig. 6 Images from sparse reconstruction with known number of targets

completely. The existing path-loss compensation model generated a highly cluttered image despite its encouraging attempt to detect the second target (Fig. 6b). Meanwhile, assuming known number of targets, the proposed model performed well by efficiently detecting all targets (Fig. 6c). Negligible clutter from our result may be originated from the algorithm for isolating clutter. Furthermore, using 100 Monte Carlo runs, SCR for existing and proposed models were 37.44 dB and 61.21 dB, respectively, whereas RCP for these models was 6.08 dB and 28.81 dB, respectively. From both metrics, we apparently recognize that the proposed model surpasses the existing model significantly.

Figure 6d shows that the existing model detected all two targets (PD of 100%) until the intensity threshold increased above 0.5, where the model could not detect the second (farthest) target. The proposed model, however, maintained the PD of 100% up to the intensity threshold of 0.7, after which the PD degraded to 50%. In essence, the proposed model can attain an acceptable value of the detection probability to recover all targets with considerably higher intensity.

Simulations were also performed under the assumption of unavailable prior information on the number of targets. From the simulations, we empirically established that choosing γ between 0.5% and 1.0% produced more satisfactory results. This choice is fairly reasonable because sparsity of the scene is uncompromised. Figure 7a shows a reconstructed image using the proposed model when the maximum number of targets was assumed to be only 0.5% of the pixel-grid size.

Comparing the images in Figs. 6b and 7, the results apparently show that, even when the number of targets is unknown, the proposed model outperforms the existing one,
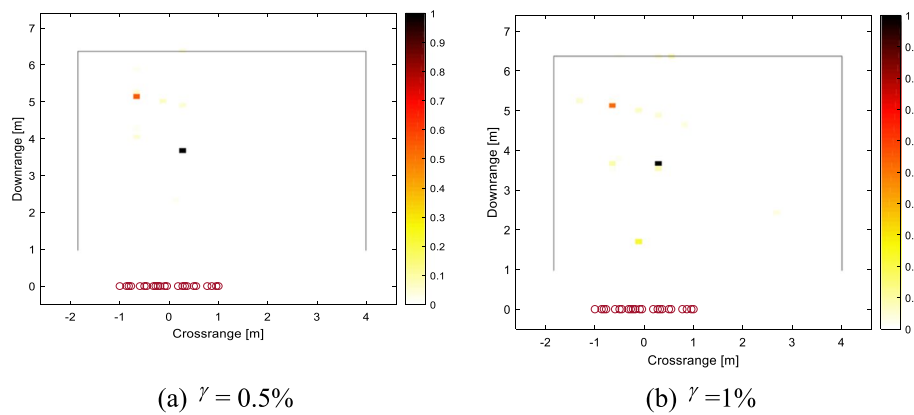
(a) $\gamma = 0.5\%$ (b) $\gamma = 1\%$

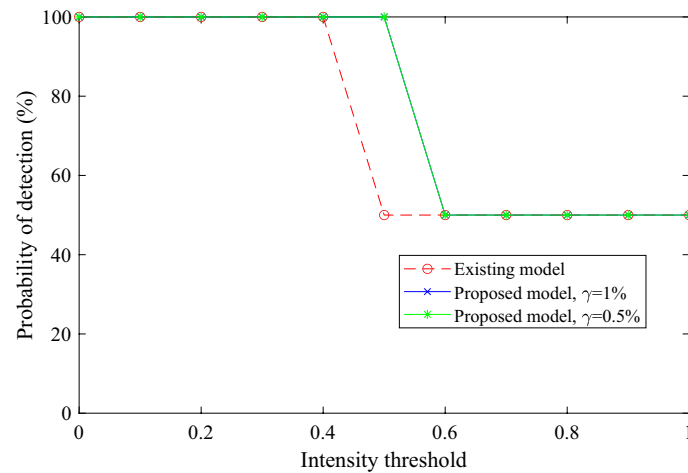**Fig. 7** Sparse reconstruction for two unknown targets

Fig. 8 PD for unknown number of targets in two targets scenario

especially when $\gamma = 0.5\%$ as its corresponding image contains relatively little clutter. SCR and RCP averaged over 100 Monte Carlo runs were, respectively, as follows: (37.44, 6.08) dB, existing model; (47.56, 21.79) dB at $\gamma = 1\%$ and (54.08, 23.64) dB at $\gamma = 0.5\%$, proposed model.

The PD line chart depicted by Fig. 8 shows that, for the existing model, the PD is maintained at 100% from intensity threshold of 0.0 up to 0.5, after which it falls to 50%. For the compensated model with $\gamma = 0.5\%$ and $\gamma = 1.0\%$, the PD was observed to coincide; the PD started at 100% and dropped to 50% above the 0.6 intensity threshold. Overall, the PD achieved by the proposed model was higher than the PD generated by the existing model.

5.2 Three targets scenario

Evaluating further the performance of our model, a three-target scene was simulated. For benchmarking purposes, we firstly applied DSBF with full measurement set. The original scene is depicted in Fig. 9a. When path-loss was not compensated, the beamformed image appeared with two distant targets hardly visible (Fig. 9b). Figure 9c
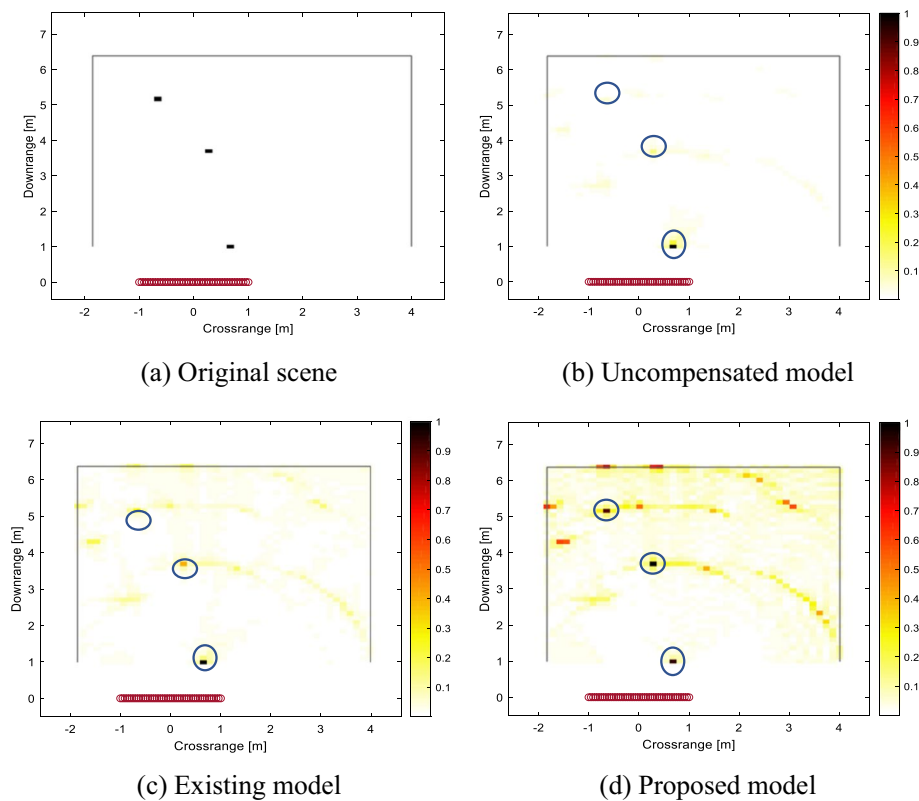
(a) Original scene

(b) Uncompensated model

(c) Existing model

(d) Proposed model

Fig. 9 Images from Delay-and-Sum Beamforming in three target scenario

presents results when the existing model was used to compensate path-loss. Apparently, results from this Figure show that the farthest target is hardly noticeable and that the middle target appears faint. This result suggests that the existing model did not adequately recoup the path-loss. However, the proposed model demonstrates its superiority by detecting all three targets with high intensity (Fig. 9d).

The PD line chart in Fig. 10 delineates the performance in detecting targets at different intensity thresholds. The uncompensated case shows poor performance as it was able to detect the three targets (PD=100%) only when the intensity was below 0.1. Between the intensity of 0.1 and 0.3, only two targets were detected (PD=66%) and above 0.3 intensity only one target was detected (PD=33%). This result explains why the two farthest targets in Fig. 9b are almost imperceptible visually. The existing model shows slight improvement by detecting all three targets below 0.3 intensity and by detecting two targets between 0.3 and 0.5 intensities. Nevertheless, beyond 0.5 intensity threshold, only one target was detected by the existing model. But the proposed model exhibited superior performance by maintaining the PD at 100% for all intensities below 0.9 intensity threshold.

With DSBF, SCR values obtained were 33.51 dB, 30.55 dB, and 26.59 dB for uncompensated case, existing model, and proposed model, respectively. RCP values were 6.58 dB, 6.02 dB, and 1.15 dB for the uncompensated, existing, and proposed model, respectively. Due to the presence of ghosts in the image, SCR and RCP did not improve for both existing and proposed models.
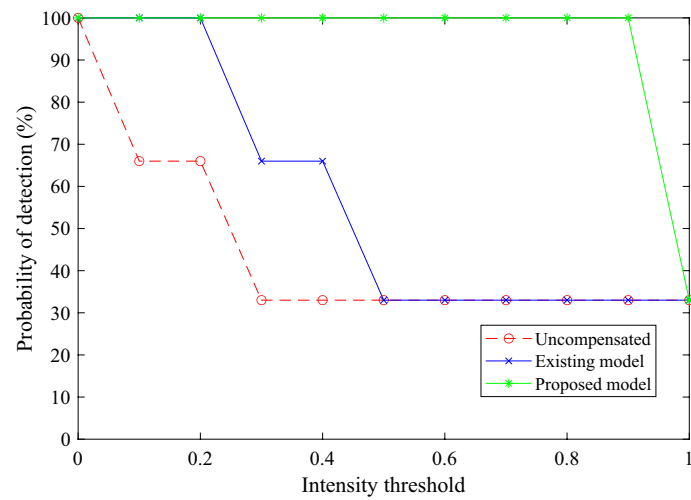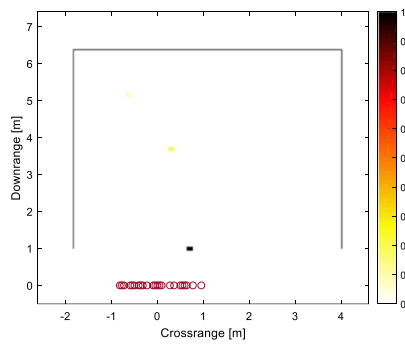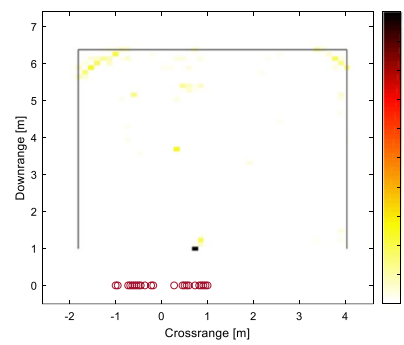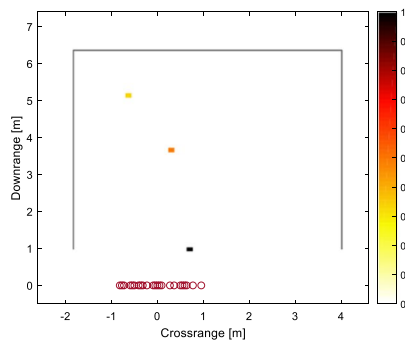
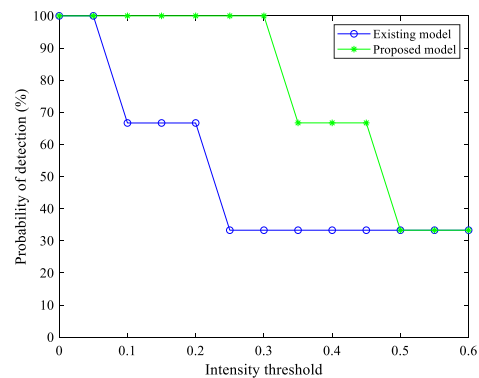**Fig. 10** PPD vs intensity threshold using DSBF for three target scenario

(a) Uncompensated model

(b) Existing model

(c) Proposed model

(d) Probability of detection

Fig. 11 Sparse reconstruction for three known targets

More simulations for the three-target scenario were carried out using multipath exploitation with CS in two main categories: known and unknown number of targets. The same data compression ratio of 25% was maintained. The reconstructed images when the number of targets is known a priori are shown in Fig. 11a through c.

Figure 11a shows the image obtained when path-loss effects were ignored, resulting in the two farthest targets being barely visible. In Fig. 11b, the existing model generates visible targets but with highly cluttered image of low intensity caused by uniform compensation. Figure 11c depicts a reconstructed image from the proposed model, in which the targets are clearly visible with unnoticeable clutter.

The PD trend is depicted in Fig. 11d. The PD for the existing model is 100% only for intensity thresholds below 0.1. In contrast, the proposed model maintains a PD of 100% up to 0.35 intensity threshold. Under this condition, the existing model detects only one target (PD=33%) whereas the proposed model detects two targets (PD=67%) until the intensity threshold of 0.5, beyond which only one target can be detected. The values of SCR for the existing and proposed models averaged over 100 Monte Carlo runs were 35.32 dB and 61.69 dB, respectively. Similarly, RCP values were 7.18 dB and 29.57 dB for the existing and the proposed model, respectively.

Figure 12 shows images obtained when the proposed model was simulated under unknown number of targets. Figure 12a shows an image from the proposed model with $\gamma = 0.5\%$ (the number of targets is 0.5% of the pixel-grid size). Likewise, Fig. 12b depicts a reconstructed image when $\gamma = 1\%$. Comparing Figs. 11b and 12, the proposed model exhibits a superior performance. Additionally, the image in Fig. 12a has less clutter than that of Fig. 12b, signifying that for this scenario, $\gamma = 0.5\%$ is a better estimation of the number of targets. SCR and RCP averaged over 100 Monte Carlo runs were, respectively, as follows: 35.32 dB and 7.18 dB, existing model; 39.54 dB and 7.96 dB ($\gamma = 1\%$), proposed model; 39.96 dB and 8.43 dB ($\gamma = 0.5\%$), proposed model. While the existing model managed to detect all targets below 0.1 intensity threshold, the proposed model performed much better (Fig. 13). With $\gamma = 1\%$, all targets were detected till 0.3 intensity threshold, whereas $\gamma = 0.5\%$ could maintain a PD of 100% until the intensity threshold reached 0.35.

6 Conclusion

This study has introduced a more effective path-loss compensation model in TWRI. The model contains two key components that facilitate generation of highly resolved images that can more accurately represent the scene of interest. The free space path-loss exponent incorporated into the compensation model ensures that targets are reconstructed
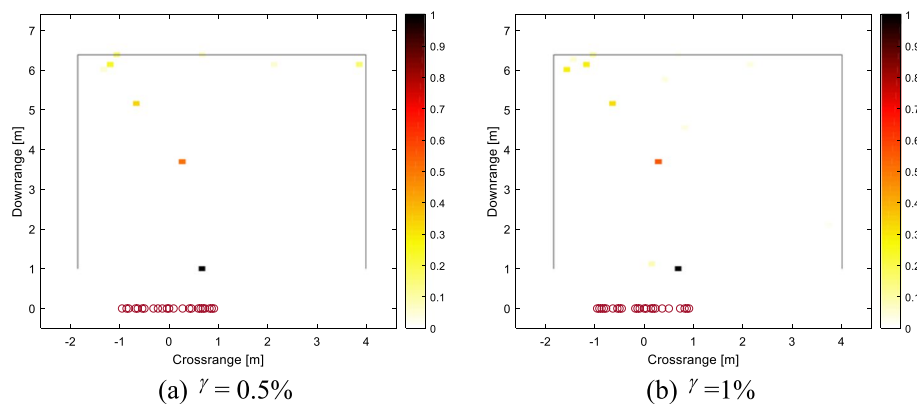

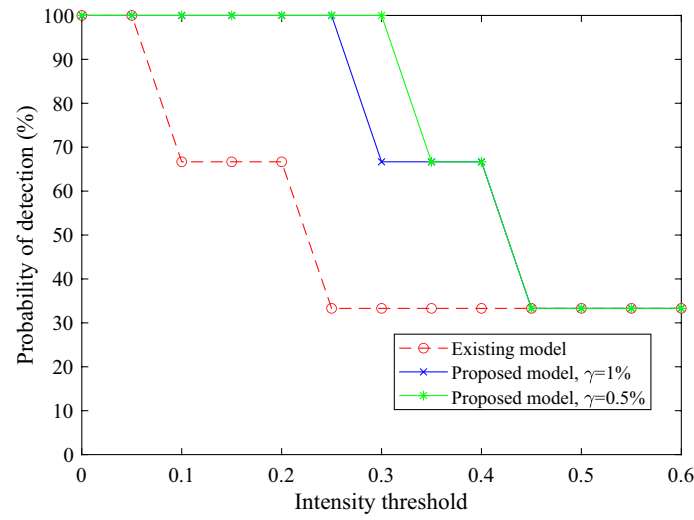**Fig. 12** Sparse reconstruction for two unknown targets

Fig. 13 Probability of detection for three unknown targets

with higher intensity. Furthermore, the proposed algorithm to isolate residual clutter when compensating path-loss guarantees high quality and almost clutter-free images. The overall outcome is that the probability of detecting targets is improved significantly. This outcome is beneficial for TWRI applications that require precise representation of the scene, including search and rescue operations. In addition, compelling features of our model may facilitate sensitive law enforcement operations. Results of the current study can be further extended by developing an experimental model to establish a suitable path-loss exponent for TWRI scenarios and by including other propagation effects, such as shadowing. Moreover, the method of estimating the number of targets behind the wall can be improved.

Appendix A: TWRI path-loss equation

Free space path-loss is expressed as the ratio of transmitted power to the received power, and is deduced from the Friis transmission Eq. (2.1). In multipath exploitation, target returns are calculated based on time delay. Since the distance covered by a signal is directly proportional to its propagation delay, the distance from the pixel to the transceiver can be expressed as

$$d_{pn} = ct_{pn}, \tag{A.1}$$

where t_{pn} is the propagation delay between the pth pixel and the nth transceiver, and c is the speed of light in free space. Because a stepped frequency radar is used to image the through-the-wall scene, the frequency range is split into frequency bins. Substituting (A.1) into (2.1) yields

$$L(m, n, p) = K(t_{pn} f_m)^2 \tag{A.2}$$

with

$$K = \frac{(4\pi)^2}{G_t G_r}. \tag{A.3}$$

K is a constant and, since normalization is performed when reconstructing the image, (A.2) can be relaxed to

$$L(m, n, p) = (t_{pn}f_m)^2. \tag{A.4}$$

Equation (A.3) is used as a basis for computing path-loss during simulation.

Appendix B: Performance evaluation metrics

B.1 Signal-to-clutter ratio (SCR)

SCR is defined as the ratio of maximum target amplitude to average amplitude in the clutter region. This metric is expressed in logarithmic notation by Leigsnering et al. [22] as

$$\text{SCR} = 20 \log_{10} \left(\frac{\max_{p \in A_t} |s(p)|}{\frac{1}{N_c} \sum_{p \in A_c} |s(p)|} \right), \tag{B.1}$$

where A_t and A_c denote target and clutter areas, respectively, $s(p)$ stands for the signal value corresponding to the pth pixel and N_c is the number of clutter pixels.

B.2 Signal-to-clutter peak (RCP)

RCP, calculated as

$$\text{RCP} = 20 \log_{10} \left(\frac{\max_{p \in A_t} |s(p)|}{\sum_{p \in A_c} |s(p)|} \right), \tag{B.2}$$

signifies how easily a target can be discerned amidst the surrounding clutter.

B.3 PD

Probability of Detection, expressed as

$$\text{PD} = \frac{\text{Detected number of true targets}}{\text{Total numberof true targets}} \times 100, \tag{B.3}$$

denotes the proportion of detected number of true targets with respect to the total number of true targets at a given intensity.

Abbreviations

CS	Compressive sensing
DSBF	Delay-and-sum beamforming
PD	Probability of detection
RCP	Relative clutter peak
SCR	Signal-to-clutter ratio
TWRI	Through-the-wall radar imaging

Declarations

Ethics approval and consent to participate
Not applicable.

Consent for publication
Not applicable.

Competing interests
The authors declare that they have no competing interests.

References

1. A.T. Abdalla, M.T. Alkhodary, A.H. Muqaibel, Multipath ghosts in through-the-wall radar imaging: challenges and solutions. ETRI J. **40**(3), 376–388 (2018)
2. M.G. Amin, *Through-the-wall radar imaging*. CRC press (2017)
3. Y. Yang, Fathy AE: see-through-wall imaging using ultra wideband short-pulse radar system. IEEE Antennas Propag. Soc. Int. Symp. **2005**, 334–337 (2005)
4. A. Kilic, I. Babaoglu, A. Babalik, A. Arslan, Through-wall radar classification of human posture using convolutional neural networks. Int. J. Antennas Propag. **2**019 (2019)
5. M.A. Maisto, M. Masoodi, R. Pierri, R. Solimene, Sensor arrangement in through-the wall radar imaging. IEEE Open J. Antennas Propag. **3**, 333–341 (2022)
6. L. Qu, C. Wang, T. Yang, L. Zhang, Y. Sun, Enhanced through-the-wall radar imaging based on deep layer aggregation. IEEE Geosci. Remote Sens. Lett. **19**, 1–5 (2022)
7. Y. Wang, Y. Zhang, M. Xiao, H. Zhou, Q. Liu, J. Gao, Physical model-driven deep networks for through-the-wall radar imaging. Int. J. Microw. Wirel. Technol. 1–8 (2022)
8. Q. Wu, Z. Lai, M.G. Amin, Through-the-wall radar imaging based on Bayesian compressive sensing exploiting multipath and target structure. IEEE Trans. Comput. Imaging **7**, 422–435 (2021)
9. R. Cicchetti, S. Pisa, E. Piuzzi, E. Pittella, P. D'Atanasio, O. Testa, Numerical and experimental comparison among a new hybrid FT-MUSIC technique and existing algorithms for through-the-wall radar imaging. IEEE Trans. Microw. Theory Tech. **69**(7), 3372–3387 (2021)
10. A.S. Barzegar, A. Cheldavi, S.H. Sedighy, V. Nayyeri, 3-D through-the-wall radar imaging using compressed sensing. IEEE Geosci. Remote Sens. Lett. **19**, 1–5 (2021)
11. Z. Lai, Q. Wu, M.G. Amin, *Through-the-wall radar imaging by exploiting multipath propagation and structure of target scene* (2021)
12. F.H.C. Tivive, A. Bouzerdoum, Toward moving target detection in through-the-wall radar imaging. IEEE Trans. Geosci. Remote Sens. **59**(3), 2028–2040 (2020)
13. H. Li, G. Cui, S. Guo, L. Kong, X. Yang, Human target detection based on FCN for through-the-wall radar imaging. IEEE Geosci. Remote Sens. Lett. **18**(9), 1565–1569 (2020)
14. F.H.C. Tivive, A. Bouzerdoum, Clutter removal in through-the-wall radar imaging using sparse autoencoder with low-rank projection. IEEE Trans. Geosci. Remote Sens. **59**(2), 1118–1129 (2020)
15. A. Salehi-Barzegar, A. Cheldavi, V. Nayyeri, A. Abdolali, A fast diffraction tomography algorithm for 3-D through-the-wall radar imaging using nonuniform fast Fourier transform. IEEE Geosci. Remote Sens. Lett. (2020)
16. A. Salehi Barzegar, A. Cheldavi, Three dimensional through the wall radar imaging using compressed sensing. In: *Radar*, vol. 7, Imam Hussein University, pp. 111–118 (2020)
17. A.S. Alahmed, O.T. Alafif, A.H. Muqaibel, A.T. Abdalla, Path-loss compensation in through-the-wall radar imaging. In *2016 International Conference on Radar, Antenna, Microwave, Electronics, and Telecommunications (ICRAMET)*, (IEEE, 2016) pp. 144–148
18. E. Kokumo, B. Maiseli, A. Abdalla, Target-to-target interaction in through-the-wall radars under path loss compensated multipath exploitation-based signal model for sparse image reconstruction. Tanzan. J. Sci. **45**(3), 382–391 (2019)
19. Y. Ma, H. Hong, X. Zhu, Interaction multipath in through-the-wall radar imaging based on compressive sensing. Sensors **18**(2), 549 (2018)
20. S. Guo, X. Yang, G. Cui, Y. Song, L. Kong, Multipath ghost suppression for through-the-wall imaging radar via array rotating. IEEE Geosci. Remote Sens. Lett. **15**(6), 868–872 (2018)
21. M. Leigsnering, *Sparsity-based multipath exploitation for through-the-wall radar imaging*. Springer (2018)

22. M. Leigsnering, F. Ahmad, M. Amin, A. Zoubir, Multipath exploitation in through-the-wall radar imaging using sparse reconstruction. IEEE Trans. Aerosp. Electron. Syst. **50**(2), 920–939 (2014)
23. Y.S. Yoon, M.G. Amin, Compressed sensing technique for high-resolution radar imaging. In *Signal Processing, Sensor Fusion, and Target Recognition XVII*, vol. 6968, (SPIE, 2008) pp. 506–515
24. M. Amin, F. Ahmad, Compressive sensing for through-thewall radar imaging. J. Electron. Imaging **22**(3), 030 (2013)
25. W. Liang, H. Xiaotao, Z. Zhimin, S. Qian, Research on UWB SAR image formation with suppressing multipath ghosts. In: *2006 CIE International Conference on Radar*, IEEE 1–3 (2006)
26. P. Setlur, M. Amin, F. Ahmad, Multipath model and exploitation in through-the-wall and urban radar sensing. IEEE Trans. Geosci. Remote Sens. **49**(10), 4021–4034 (2011)
27. E. Lagunas, M.G. Amin, F. Ahmad, M. Nájar, Joint wall mitigation and compressive sensing for indoor image reconstruction. IEEE Trans. Geosci. Remote Sens. **51**(2), 891–906 (2012)
28. F.H.C. Tivive, M.G. Amin, A. Bouzerdoum, Wall clutter mitigation based on eigen-analysis in through-the-wall radar imaging. In: *2011 17th International Conference on Digital Signal Processing (DSP)*, IEEE 1–8 (2011)
29. D.L. Donoho, Compressed sensing. IEEE Trans. Inf. Theory **52**(4), 1289–1306 (2006)
30. J. Romberg, Imaging via compressive sampling. IEEE Signal Process. Mag. **25**(2), 14–20 (2008)
31. M. Leigsnering, F. Ahmad, M.G. Amin, A.M. Zoubir, Compressive sensing-based multipath exploitation for stationary and moving indoor target localization. IEEE J. Sel. Top. Signal Process. **9**(8), 1469–1483 (2015)
32. E. Lagunas, M.G. Amin, F. Ahmad, M. Nájar, Wall mitigation techniques for indoor sensing within the compressive sensing framework. In: *IEEE 7th Sensor Array and Multichannel Signal Processing Workshop (SAM). 2012*, 213–216 (2012)
33. M. Mabrouk, S. Rajan, M. Bolic, I. Batkin, H.R. Dajani, V. Z. Groza, Detection of human targets behind the wall based on singular value decomposition and skewness variations. In: IEEE Radar Conference. IEEE **2014**, 1466–1470 (2014)
34. A.H. Muqaibel, A.T. Abdalla, M.T. Alkhodary, S. Al-Dharrab, Aspect-dependent efficient multipath ghost suppression in TWRI with sparse reconstruction. Int. J. Microw. Wirel. Technol. **9**(9), 1839–1852 (2017)
35. J. Yang, Y. Zhang, *Alternating direction algorithms for in compressive sensing.* Tech. rep., Technical report, 2010. 2 (2010)
36. F. Ahmad, M.G. Amin, S.A. Kassam, A beamforming approach to stepped-frequency synthetic aperture through-the-wall radar imaging. In: *1st IEEE International Workshop on Computational Advances in Multi-Sensor Adaptive Processing, 2005.*, IEEE 24–27 (2005)
37. A.A. AlBeladi, A.H. Muqaibel, Evaluating compressive sensing algorithms in through-the-wall radar via F1-score. Int. J. Signal Imaging Syst. Eng. **11**(3), 164–171 (2018)

Publisher's Note